



UNIVERSITEIT•STELLENBOSCH•UNIVERSITY  
jou kennisvenoot • your knowledge partner

*Design and comparison of three surface-mounted PM motors for a light electric vehicle*

---

**Article:**

F. Du Plessis, S. Pastellides and R.-J. Wang, "Design and comparison of three surface-mounted PM motors for a light electric vehicle," *2021 Southern African Universities Power Engineering Conference/Robotics and Mechatronics/Pattern Recognition Association of South Africa (SAUPEC/RobMech/PRASA)*, pp.1-6, 27-29 Jan. 2021, Potchefstroom, South Africa

<http://dx.doi.org/10.1109/SAUPEC/RobMech/PRASA52254.2021.9377239>

---

**Reuse**

Unless indicated otherwise, full text items are protected by copyright with all rights reserved. Archived content may only be used for academic research.

# Design and Comparison of Three Surface-Mounted PM Motors for a Light Electric Vehicle

Francois Du Plessis<sup>†</sup>, Stavros Pastellides<sup>†</sup> and Rong-Jie Wang<sup>\*</sup>

Department of Electrical and Electronic Engineering

Stellenbosch University

Matieland 7602, South Africa

Email: 20688830@sun.ac.za<sup>†</sup>, 17509955@sun.ac.za<sup>†</sup>, rwang@sun.ac.za<sup>\*</sup>

**Abstract**—Electric vehicles (EV) are increasingly used in both urban and industrial environments. Electric motors are the essential part of the EV power train systems. Different types of electric motor technologies have been developed for the purpose. Amongst others, permanent magnet synchronous motors (PMSM) are widely used for EV applications because of their unique advantages such as high efficiency and high power density. This paper presents the optimal design of three different surface-mounted PMSMs with fractional-slot tooth-concentrated and distributed winding topologies, respectively. The performance comparison of these motors will outline their respective advantages and disadvantages.

**Index Terms**—Design optimization, finite element analysis, permanent magnet machines, rotating machines, traction motors

## I. INTRODUCTION

High performance electric motors are one of the critical components needed for the widespread adoption of electric vehicles (EVs). Substituting conventional field windings with permanent magnets (PM) gives the advantage of reduced copper losses and increased reliability due to the removal of brushes [1]. There are two main types of PM machines, namely surface-mounted and interior PM machines.

The main advantages offered by the surface-mounted PM (SPM) machine, shown in Fig. 1a, include better manufacturability (low cost) and high PM utilisation factor (less leakage flux) [1], [2]. As the rare-earth type PMs have a permeability very close to air the d- and q-axis inductances of a SPM motor are identical (non-salient) [1], [2]. This may have control and operational implications but high quality torque and electromotive force (EMF) are produced [2]. The major disadvantage of SPM motors is the risk of demagnetization due to the direct exposure of the PMs to the stator fields [1]. The SPM motors may feature integer-slot or fractional-slot type of windings. The latter includes both the tooth-concentrated and distributed winding layouts.

The tooth-wound fractional-slot concentrated windings (FSCW), including alternate tooth-wound (single-layer) or all tooth-wound (double-layer), offer various advantages such as high power density, low copper losses (short end-turns), low

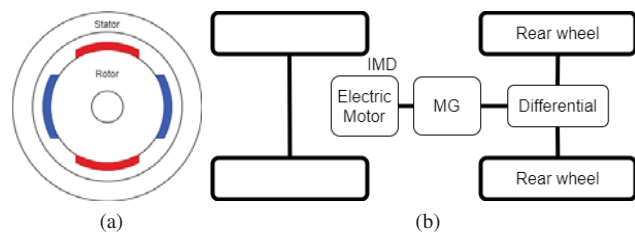


Fig. 1. (a) Four-pole SPM machine, (b) power train system layout of LEV

cogging torque, good flux weakening capability and fault tolerance [3], [4].

In this paper three different fractional-slot SPM motors with tooth-concentrated and distributed winding topologies are optimally designed for a light electric vehicle (LEV) application. Their performance characteristics and costs are extensively compared, which will outline their respective advantages and disadvantages. The remainder of the paper is organized as follows: In Section II an overview of traction efforts and vehicle specifications is given. Section III describes the field-circuit coupled design optimisation procedure for the candidate machines. Section IV compares the performance characteristics of the three optimally designed machines. Relevant conclusions are drawn in Section V.

## II. VEHICLE AND MOTOR SPECIFICATIONS

The power train system of the LEV is shown in Fig. 1b. It features an integrated motor drive connected to a mechanical differential through a magnetic gear with a fixed transmission ratio,  $i_g$ . The maximum output torque of the motor  $T_{p(base)}$ , is limited by the maximum output torque of the magnetic gear,  $T_{MG(max)}$ . Based on the vehicle physics model described in [5] along with the specifications of the vehicle and drive train given in Table I, the motor torque and speed requirements can be determined as in Table II. Additional specifications are based on inverter and dimensional constraints and are summarised in Table II along with the magnet and core material used.

TABLE I  
DIMENSIONS AND SPECIFICATIONS OF EV DRIVE TRAIN

Parameter	Value
Wheel radius [ $r_d$ ]	0.299 m
Frontal area [ $A_f$ ]	2.5 m <sup>2</sup>
Aerodynamic drag coefficient [ $C_D$ ]	0.3
Rolling resistance coefficient [ $f_r$ ]	0.013
Grading percentage	0%
Vehicle mass [ $M_v$ ]	1000 kg
Maximum vehicle speed [ $V_{v(max)}$ ]	50 km/h
MG ratio [ $i_g$ ]	11:1
Maximum MG torque [ $T_{MG(max)}$ ]	254 Nm

TABLE II  
DIMENSIONS AND SPECIFICATIONS OF SPM

Parameter	Value
Outer diameter [ $D_{out(max)}$ ]	212 mm
Shaft diameter [ $D_{shaft}$ ]	30 mm
Output power [ $P_{out}$ ]	3 kW
Maximum RMS voltage [ $V_{LL}$ ]	48 V <sub>LL</sub>
Maximum RMS phase current [ $I_S$ ]	44 A
Peak losses [ $P_{loss}$ ]	300 W
Base speed [ $N_{p(base)}$ ]	1500 rpm
Maximum speed [ $N_{p(max)}$ ]	5000 rpm
Torque at base speed [ $T_{p(base)}$ ]	19.1 Nm
Torque at maximum speed [ $T_{p(max)}$ ]	5.73 Nm
PM material	NdFeB N48H
PM remnant flux density [ $B_r$ @ 80°C]	1.2899 T
PM recoil permeability [ $\mu_r$ ]	1.05
Core material	M19_26G

### III. DESIGN PROCEDURE

#### A. Pole and slot combinations

For the specific LEV drive train configuration, the maximum motor speed is specified as 5000rpm. To ensure a good efficiency at high speed, the maximum electrical frequency of the motor is constrained to approximately 400 Hz. Considering also the winding symmetry conditions, the following pole and slot combinations are selected for the SPM motor design study, i.e. 12-slot 10-pole single-layer winding (12s10p(S)), 12-slot 10-pole double-layer winding (12s10p(D)) and 36-slot 8-pole double-layer winding (36s8p(D)). As shown in Table III, all these machines offer high fundamental winding factors and low harmonic winding factors.

#### B. Design procedure and initial machine sizing

The flowchart of analytical motor design and sizing procedure is shown in Fig. 2. The initial sizing procedure from [6] is employed, which requires choosing certain parameters

TABLE III  
WINDING FACTORS OF THE SELECTED MACHINES

Configuration	12s10p(S)	12s10p(D)	36s8p(D)
$\nu = 1$	0.966	0.933	0.945
$\nu = 5$	0.259	0.067	0.140
$\nu = 7$	0.259	0.067	-0.061

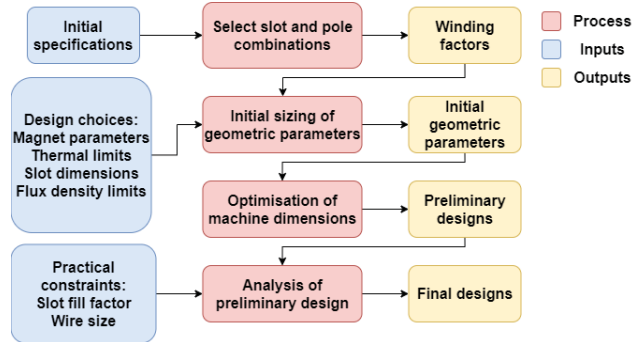


Fig. 2. Machine design process

TABLE IV  
MACHINE SIZING PARAMETERS

Parameter	12s10p(S)	12s10p(D)	36s8p(D)
Magnet thickness [ $h_m$ ]	3 mm	3 mm	2 mm
Slot opening [ $b_{s0}$ ]	2 mm	2 mm	2 mm
Electrical frequency [f]	125 Hz	125 Hz	100 Hz
Air gap [g]	1 mm	1 mm	1 mm
Pole coverage ratio [ $\alpha_p$ ]	0.83	0.83	0.83
Fill factor [ $f_f$ ]	35%	35%	35%
Winding factor [ $K_{w1}$ ]	0.966	0.933	0.945

as shown in Tables II and IV for the initial design process. In addition, the linear current density  $K_s$  and current density  $J$  are chosen as 35 kA/m and 4 A/mm<sup>2</sup>, respectively. In this way thermal constraints are inherently considered. Magnetic saturation is considered by the choice of  $B_{ys(max)}$  and  $B_{ts(max)}$  as 1 T and 1.6 T, respectively. Note the initial machine sizing is performed at base speed. First, the air-gap flux density is calculated. It is approximated as a square wave with amplitude  $B_g$ , shown in (1), with a fundamental sinusoidal component  $B_{g1}$ , given by (2). The Carter factor  $K_c$  is assumed to be 1.05. The torque at base speed can be calculated from (3), where  $D_{ag}$  and  $L$  are the air-gap diameter and stack length, respectively.

$$B_g = B_r \frac{h_m}{\frac{h_m}{\mu_r} + gK_c} \quad (1)$$

$$B_{g1} = \frac{4}{\pi} B_g \sin\left(\frac{\alpha_p \pi}{2}\right) \quad (2)$$

$$T_{p(base)} = \frac{\sqrt{2}\pi}{4} B_{g1} K_s D_{ag}^2 L \quad (3)$$

The stator yoke thickness,  $h_{ys}$ , and tooth width,  $w_{tt}$ , can be calculated from (4) and (5) respectively, where  $\tau_p$  is the pole pitch,  $\tau_s$  the slot pitch and  $k_j$  the lamination stacking factor. In the case of FSCW machines where the PM circumference is comparable to the slot pitch, (6) and (7) must be used to account for the flux shunting effect between two adjacent magnets [6].

$$h_{ys} = \frac{B_g \alpha_p \tau_p}{2B_{ys(max)} k_j} \quad (4)$$

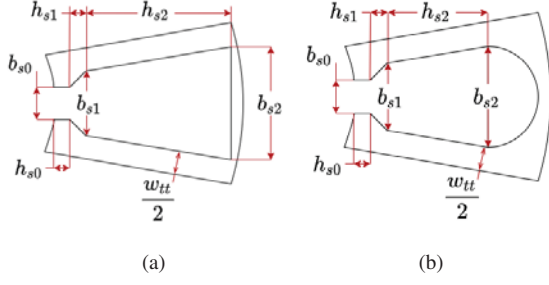


Fig. 3. Stator slot dimensions: (a) trapezoidal slot (b) round slot

$$w_{tt} = \frac{B_g \tau_s}{B_{ts(max)} k_j} \quad (5)$$

$$h_{ys} = \frac{B_g}{B_{ys(max)} k_j} \left( \alpha_p \tau_p - \frac{\tau_s - \tau_p}{2} \right) \quad (6)$$

$$w_{tt} = \frac{B_g}{B_{ts(max)} k_j} \left( \alpha_p \tau_p - \frac{\tau_s - \tau_p}{2} \right) \quad (7)$$

Furthermore,  $D_{h1}$  is defined by (8), while slot enclosure dimensions  $h_{s0}$  and  $h_{s1}$  (shown in Fig. 3a) are chosen as 2 mm each. The slot width,  $b_{s1}$ , is calculated by (9) assuming a constant tooth width, where  $Q_s$  is the number of stator slots.

$$D_{h1} = D_{is} + h_{s0} + h_{s1} \quad (8)$$

$$b_{s1} = \frac{\pi D_{h1}}{Q_s} - w_{tt} \quad (9)$$

The usable stator slot area  $A_{us}$  is calculated from (10). The stator slot height  $h_{us}$  and the bottom slot width  $b_{s2}$  are calculated using (11) and (12), respectively. The initial machine sizing procedure assumes a trapezoidal slot shape as in Fig. 3a. However, in the final design round slots as shown in Fig. 3b are used.

$$A_{us} = \frac{\pi D_{h1} K_s}{J Q_s K_{w1} f} \quad (10)$$

$$h_{s2} = \frac{-b_{s1} + \sqrt{b_{s1}^2 + \left( \frac{4\pi A_{us}}{Q_s} \right)}}{\frac{2\pi}{Q_s}} \quad (11)$$

$$b_{s2} = \left[ \frac{\pi(D_{h1} + 2h_{s2})}{Q_s} \right] - w_{tt} \quad (12)$$

The number of turns per phase  $N_{ph}$  can be calculated using (13) assuming a constant magnet thickness [7], where  $E_m$  is assumed equal to the line-to-neutral phase voltage value,  $L' = L + 2g$  and  $\omega_e$  is the angular electrical frequency in rad/s. To ensure an integer number of conductors per slot  $z_Q$ ,  $N_{ph}$  must be chosen appropriately in (14), with  $z_c$  the number of coils per phase.

$$N_{ph} = \frac{\sqrt{2} E_m}{\omega_e K_{w1} \alpha_p B_{g1} \tau_p L'} \quad (13)$$

$$z_Q = \frac{N_{ph}}{z_c} \quad (14)$$

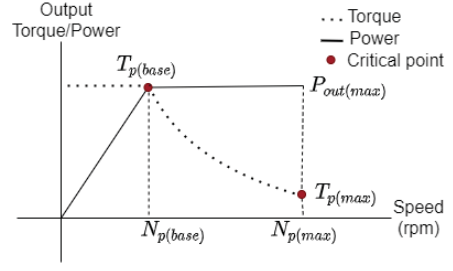


Fig. 4. Torque and power characteristic over speed range

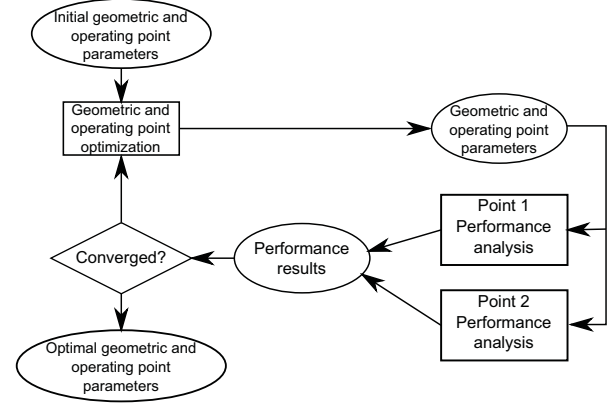


Fig. 5. Machine dimension optimisation process

### C. Machine optimisation

The optimisation strategy employed analyses the two critical operating points,  $N_{p(base)}$  and  $N_{p(max)}$ , which are the base and maximum speeds as shown in Fig. 4. By imposing performance constraints at these critical points throughout the optimisation, a constant power speed range (CPSR) will be ensured. Adopting the strategy proposed in [2], [8], the optimisation problem is formulated as:

$$\begin{aligned} \text{Minimise: } & F(\mathbf{x}) = C_{total} \\ \text{Subject to: } & T_{p(base)} \geq 19.1 \text{ Nm} & T_{p(max)} \geq 5.73 \text{ Nm} \\ & V_{LL(base)} \leq 48 \text{ V} & V_{LL(max)} \leq 48 \text{ V} \\ & I_{S(base)} \leq 42.5 \text{ A} & I_{S(max)} \leq 42.5 \text{ A} \\ & P_{loss(base)} \leq 265 \text{ W} & P_{loss(max)} \leq 265 \text{ W} \\ & B_{MM(base)} \geq 0.05 \text{ T} & B_{MM(max)} \geq 0.05 \text{ T} \end{aligned}$$

Note that  $\mathbf{x}$  is a vector containing design variables including the dq-current densities, geometric variables and coil turns [2]. The objective of the optimization is to find the least cost motor design that can satisfy the performance requirements.

The design optimisation process was implemented using SEMFEM, an in-house 2D finite element (FE) package. The process followed is illustrated in Fig. 5, starting with the initial geometric and operating point parameters obtained from the sizing process. For each operating point, certain constraints are imposed to ensure required performance, which include the required torque, the voltage and current limits and the maximum allowable losses. The demagnetisation margin

TABLE V  
MAIN PARAMETERS OF THE OPTIMUM MOTOR DESIGNS

Parameter	12s10p (S)	12s10p (D)	36s8p (D)
$D_{shaft}$	30 mm	30 mm	30 mm
$D_{ag}$	62.48 mm	72.24 mm	77.15 mm
$h_m$	4.75 mm	2.32 mm	2.5 mm
$\alpha_p$	0.75	0.7577	0.7258
$g$	1 mm	1 mm	1 mm
$D_{out}$	170.14 mm	156.76 mm	184.92 mm
$L$	108.67 mm	95.83 mm	70.21 mm
$N_{ph}$	40	44	60
$d_{wire}$	1.63 mm	1.45 mm	1.45 mm
$z_{wire}$	4	5	5
$f_f$	38.05%	38.2%	37.3%
$h_{s0}$	3.27 mm	4 mm	5.19 mm
$h_{s1}$	0 mm	0 mm	0 mm
$h_{s2}$	26 mm	22 mm	38.24 mm
$b_{s0}$	4.19 mm	3.33 mm	1.6 mm
$b_{s1}$	6.2 mm	14 mm	5 mm
$b_{s2}$	27 mm	24 mm	9.56 mm

$B_{MM}$  defines a safety margin above the *knee point* of the demagnetization curve of the PMs. For NdFeB N48H the knee point occurs at 0.2 T.

As shown in Fig. 5, the optimization is essentially of a single loop structure where the parameters of geometric and operating point are optimized. The optimisation algorithm implemented was the sequential least squares programming algorithm (SLSQP), which is a gradient-based optimisation method. To ensure a global optimum is found within the design space, the optimum design is checked with random initial variable sets.

#### IV. PERFORMANCE EVALUATION

##### A. Dimensions, cost and inductance

The dimensions and parameters of the final motor designs are shown in Table V with  $d_{wire}$ ,  $z_{wire}$  being the wire diameter and number of wires per conductor. The 12s10p (D) machine was found to have the lowest cost (Table VI), which can be attributed to shorter end turns (low copper usage) and thinner magnets. The 36s8p (D) machine uses the least amount of PM material, but largest amount of copper material among the three machines.

The inductance values of the machines are compared in Table VII. In all cases, the slot leakage inductance  $L_\sigma$ , is the dominant component. The end-winding leakage inductance  $L_{ew}$ , is negligible while the harmonic leakage inductance  $L_h$ , makes a large contribution to the synchronous inductance  $L_s$ , of the 12-slot machines. This can be attributed to the high levels of harmonic content present in these machines, which is seen clearly when evaluating their winding functions and which makes FSCW machines good candidates for flux-weakening operation [9]. The magnetising inductance  $L_m$ , makes a significant contribution to the  $L_s$  of the 36-slot machine. This is also expected, based on winding function analysis [9]. The 36-slot machine features the largest synchronous inductance, which also explains its excellent flux-weakening capability.

TABLE VI  
MASS AND COST OF THE OPTIMUM MACHINES

Material	12s10p (S)	12s10p (D)	36s8p (D)
Copper	2.31 kg	2.234 kg	3.434 kg
Magnets	0.518 kg	0.273 kg	0.221 kg
Steel	9.64 kg	6.943 kg	7.002 kg
Total Mass	12.468 kg	9.45 kg	10.657 kg
Total Cost	\$ 60.59	\$ 42.44	\$ 47.95

TABLE VII  
INDUCTANCE OF OPTIMUM MACHINES

Inductance	12s10p (S)	12s10p (D)	36s8p (D)
$L_\sigma$ ( $\mu$ H)	586.3	430.67	606.8
$L_{ew}$ ( $\mu$ H)	2.61	1.36	52.74
$L_h$ ( $\mu$ H)	178.34	115.79	7.97
$L_m$ ( $\mu$ H)	68.95	152.6	344.78
$L_s$ ( $\mu$ H)	836.2	700.43	1012.3

##### B. Main performance characteristics

The performance characteristics of the three optimum machines at 1500 and 5000 rpm are summarized in Tables VIII and IX. Except for the 12s10p (S) machine at 1500 rpm, the required traction performance at each operating speed are satisfied for the optimum machines. As shown in Fig. 6, sinusoidal currents are drawn by the machines while near-sinusoidal flux linkages are obtained with flattening at the peaks. This results in back-EMF waveforms being distorted around the zero crossings, while general distortion is observed at 5000 rpm. The 12s10p (S) machine displays the lowest torque ripple among the three designs while the 36s8p (D) machine has relatively high torque ripple.

Flux-density maps of the optimum machines at 1500 and 5000 rpm are shown in Figs. 7, 8 and 9 where flux-weakening conditions can be observed at high speeds. All the machines exhibit high levels of efficiency over the entire speed range as shown on the efficiency map in Fig. 10. The loss maps of the optimum machines are also shown in Fig. 11. As can be seen, the 12-slot machines feature significantly less losses at low speeds compared to high speeds, while the 36-slot machine shows relatively similar losses over the speed range. This can be attributed to the magnet and core losses which are frequency dependent and contribute significantly to the total losses of the 12-slot machines due to the high levels of harmonic content [9]. For the 36-slot machine, the copper losses are dominant and thus total losses are less dependent on frequency. Efficiency and loss maps were generated using ANSYS Maxwell under the assumption of maximum torque per ampere (MTPA) operation.

The demagnetisation margins of the optimised machines are shown in Table X, which shows that the optimum machines operate well above the knee point.

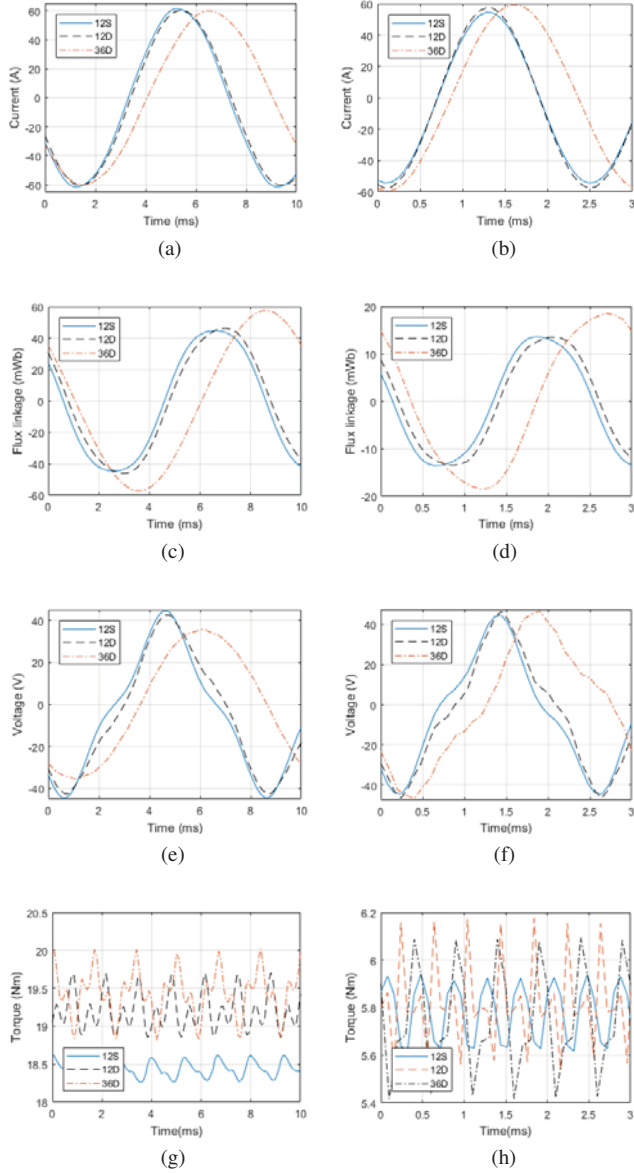


Fig. 6. (a) Phase current at 1500 rpm (b) phase current at 5000 rpm (c) flux-linkage of all designs at 1500 rpm (d) flux-linkage at 5000 rpm (e) back-EMF at 1500 rpm (f) back-EMF at 5000 rpm (g) output torque at 1500 rpm (h) output torque at 5000 rpm

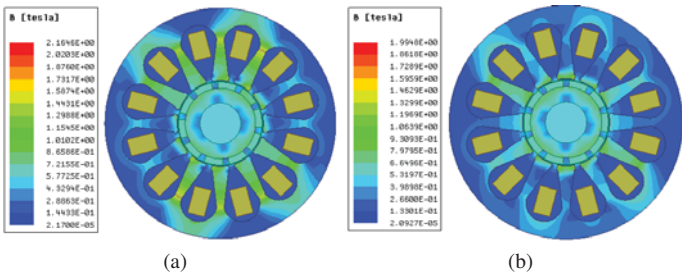


Fig. 7. Flux density of 12s10p(S): (a) 1500 rpm (b) 5000 rpm

TABLE VIII  
RESULTS AT 1500 RPM

Parameter	12s10p(S)	12s10p(D)	36s8p(D)
$T_p$	18.43 Nm	19.21 Nm	19.43 Nm
$P_{out}$	2.895 kW	3.017 kW	3.053 kW
$P_{Cu}$	175.1 W	166.94 W	251.28 W
$P_{Core}$	31.3 W	33.02 W	30.48 W
$P_{magnet}$	6.57 W	7.995 W	0.324 W
Efficiency $[\eta]$	93.15%	94.53%	92.4%
Power factor	0.8522	0.8988	0.94
$I_{s(RMS)}$	43.41 A	42.71 A	42.27 A
$\lambda_a(RMS)$	33.8 mWb	33.8 mWb	40.4 mWb

TABLE IX  
RESULTS AT 5000 RPM

Parameter	12s10p(S)	12s10p(D)	36s8p(D)
$T_p$	5.779 Nm	5.8255 Nm	5.75 Nm
$P_{out}$	3.026 kW	3.05 kW	3.01 kW
$P_{Cu}$	138.67 W	151.72 W	248.93 W
$P_{Core}$	79.66 W	56.24 W	57.09 W
$P_{magnet}$	51.04 W	55.84 W	2.08 W
Efficiency $[\eta]$	94.3%	93.79%	92.57%
Power factor	0.999	0.96	0.9298
$I_{s(RMS)}$	38.62 A	40.72 A	42.065 A
$\lambda_a(RMS)$	10.17 mWb	10.23 mWb	13.5 mWb

TABLE X  
DEMAGNETISATION MARGINS OF OPTIMISED MACHINES

Parameter	12s10p(S)	12s10p(D)	36s8p(D)
$B_{MM(base)}$	0.3072 T	0.3052 T	0.1462 T
$B_{MM(max)}$	0.2761 T	0.2933 T	0.2247 T

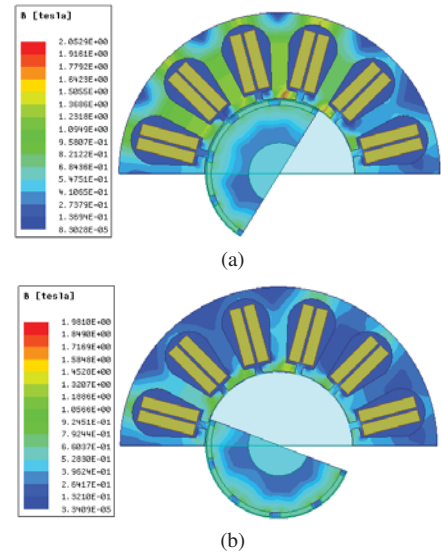


Fig. 8. Flux density of 12s10p(D): (a) 1500 rpm (b) 5000 rpm

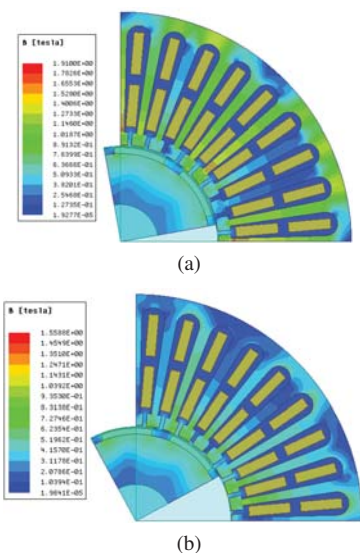


Fig. 9. Flux density of 36s8p(D): (a) 1500 rpm (b) 5000 rpm

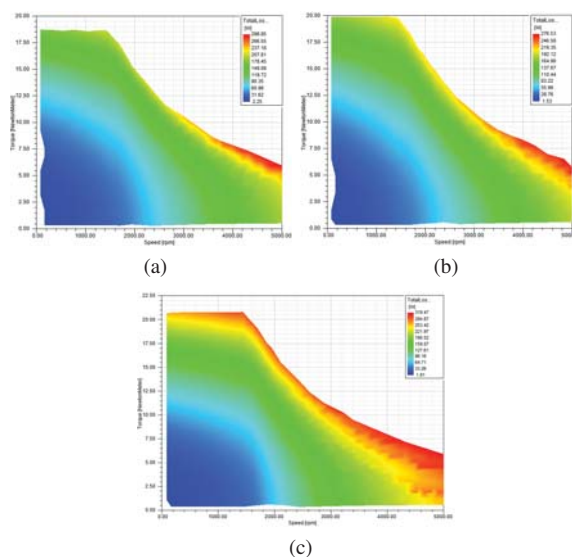


Fig. 11. Loss maps: (a) 12s10p(S) (b) 12s10p(D) (c) 36s8p(D)

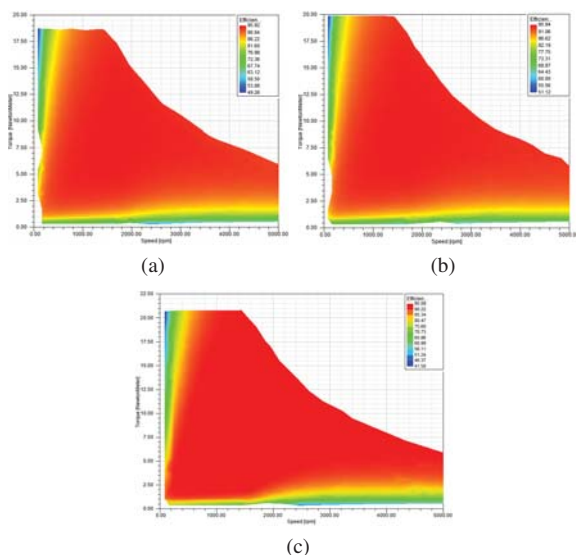


Fig. 10. Efficiency maps: (a) 12s10p(S) (b) 12s10p(D) (c) 36s8p(D)

## V. CONCLUSION

This paper described the optimal design of three fractional-slot surface-mounted PM machines and the comparison of their performances. It shows that the 12-slot 10-pole double-layer machine delivers the required performance at the lowest cost with the added benefit of ease of manufacturing. The 36-slot 8-pole machine exhibits a good flux weakening ability and wide CPSR due to its high synchronous inductance. The adopted machine sizing procedure was found to be sufficient when combined with the optimisation process. The design process delivered good overall results, proving to be an effective method.

## REFERENCES

- [1] I. D. Kakoudakis, E. K. Karamanis, I. I. Kikidis, and A. G. Kladas, "Comparison of permanent magnet motor configurations for electric

vehicle applications," in *2018 XIII International Conference on Electrical Machines (ICEM)*, 2018, pp. 2058–2064.

- [2] S. Pastellides, S. Gerber, and R.-J. Wang, "Design strategy and comparison of four PM motor topologies for a 2kW traction application," in *2019 Southern African Universities Power Engineering Conference/Robotics and Mechatronics/Pattern Recognition Association of South Africa (SAUPEC/RobMech/PRASA)*, 2019, pp. 358–363.
- [3] A. M. EL-Refaie, "Fractional-slot concentrated-windings synchronous permanent magnet machines: opportunities and challenges," *IEEE Transactions on Industrial Electronics*, vol. 57, no. 1, pp. 107–121, 2010.
- [4] Y. Tang, J. Paulides, E. Kazmin, and E. Lomonova, "Investigation of winding topologies for permanent magnet in-wheel motors," *COMPEL: The International Journal for Computation and Mathematics in Electrical and Electronic Engineering*, vol. 31, pp. 88–107, 2011.
- [5] M. Ehsani, Y. Gao, S. Gay, and A. Emadi, *Modern electric, hybrid electric, and fuel cell vehicles*. Boca Raton, Florida: CRC Press, 2004.
- [6] S. Vaschetto, A. Tenconi, and G. Bramerdorfer, "Sizing procedure of surface mounted PM machines for fast analytical evaluations," in *2017 IEEE International Electric Machines and Drives Conference (IEMDC)*, 2017, pp. 1–8.
- [7] H. Hrabovcova, T. Jokinen, and J. Pyrhonen, *Design of Rotating Electrical Machines*. John Wiley & Sons, Ltd, 2008.
- [8] S. Gerber and R.-J. Wang, "Traction motor optimization using mesh reshaping for gradient evaluation," in *2020 International Conference on Electrical Machines (ICEM)*, 2020, pp. 2546–2552.
- [9] A. M. EL-Refaie and T. M. Jahns, "Optimal flux weakening in surface PM machines using fractional-slot concentrated windings," *IEEE Transactions on Industry Applications*, vol. 41, no. 3, pp. 790–800, May/June 2005.